Article

A Coastal Flood Early-Warning System Based on Offshore Sea State Forecasts and Artificial Neural Networks

Michalis Chondros [1,2,*](ORCID), Anastasios Metallinos [1,2], Andreas Papadimitriou [1,2], Constantine Memos [1] and Vasiliki Tsoukala [1]

1   Laboratory of Harbour Works, School of Civil Engineering, National Technical University of Athens, 5 Heroon Polytechniou Str., 15780 Zografou, Greece; anast.metallinos@gmail.com (A.M.); andrewtnt@mail.ntua.gr (A.P.); cmemos@gmail.com (C.M.); tsoukala@mail.ntua.gr (V.T.)
2   Scientia Maris, Agias Paraskevis Str. 117, 15234 Chalandri, Greece
*   Correspondence: chondros@hydro.ntua.gr; Tel.: +30-21-077-21992

Abstract: An integrated methodological approach to the development of a coastal flood early-warning system is presented in this paper to improve societal preparedness for coastal flood events. The approach consists of two frameworks, namely the Hindcast Framework and the Forecast Framework. The aim of the former is to implement a suite of high-credibility numerical models and validate them according to past flooding events, while the latter takes advantage of these validated models and runs a plethora of scenarios representing distinct sea-state events to train an Artificial Neural Network (ANN) that is capable of predicting the impending coastal flood risks. The proposed approach was applied in the flood-prone coastal area of Rethymno in the Island of Crete in Greece. The performance of the developed ANN is good, given the complexity of the problem, accurately predicting the targeted coastal flood risks. It is capable of predicting such risks without requiring time-consuming numerical simulations; the ANN only requires the offshore wave characteristics (height, period and direction) and sea-water-level elevation, which can be obtained from open databases. The generic nature of the proposed methodological approach allows its application in numerous coastal regions.

Keywords: coastal flood; inundation risk; early-warning system; wave overtopping; storm surge; artificial neural network; field observations; numerical modelling

1. Introduction

Coastal floods are regarded as one of the most dangerous natural disasters that can harm coastal communities. The rapid urbanization of coastal areas in conjunction with climate change and often inadequate coastal protection infrastructure lead to increased flood risks for coastal areas. According to the recently published Intergovernmental Panel report on Climate Change [1], sea levels continue to rise at an increasing rate and the increased mean and extreme sea levels are projected to exacerbate risks for human communities in low-lying coastal areas. In addition, coastal hazards will be further exacerbated by an increase in the frequency of extreme events. Hence, local stakeholders and coastal planners are in urgent need of decision-support tools. In the long-term, these tools can be applied to the planning of risk-reduction strategies based on future scenarios of flooding events. In the short-term, the development of early-warning systems (EWS) can significantly contribute to the protection of coastal communities. In the present study, the issue under scrutiny is the latter.

The processes that drive flood risks include sea-water elevation due to astronomical tide and storm surge, and wave action, i.e., setup, runup and overtopping. In addition, climate change plays a dominant role in the mean rise in sea level and the frequency and intensity of storms and waves. The manner in which these drivers combine among themselves determines the magnitude of any flood impacts. There are many uncertainties

and variables in the physical processes that occur during a flood event, and hence many possible methodologies for treating such an event.

Recent research efforts have contributed to the understanding of coastal flood events and their drivers. Clear progress has been made in the fields of occurrence of compound events [2], i.e., surge and waves [3], the numerical modelling of wave propagation and nearshore hydraulics [4], flood water movement over land areas [5], impact of storms on coasts [6] and flood vulnerability [7]. Nevertheless, the vast majority of the relevant existing literature focuses on capturing past flood events or predicting long-term (years to decades) flood risks for large-scale coastal areas, mainly based on various climate change projections.

Fewer research efforts have been realized regarding short-term forecasts, to the best of our knowledge. Doong et al. [8] developed an operational coastal flood EWS by integrating existing sea-state-monitoring technology, numerical ocean forecasting models, historical database and experience, and computer science. de Kleermaeker et al. [9] provided an overview of the many developments that are needed for an accurate and reliable forecasting system. Bogaard et al. [10] presented an EWS modelling framework, implementing wave and hydrodynamic models to provide nearshore conditions and an additional model to derive actual on-shore effects such as wave runup. The results of this framework served as input to a decision-support system, based on a Bayesian network, to link coastal hazards to their socio-economic and environmental consequences. Dreier and Fröhle [11] developed an operational now- and forecast system, consisting of available field measurements, data from numerical wave simulations and an empirical wave run-up approach. Winter et al. [12] presented the steps in the development of an EWS of storm wave-driven flooding along coral reef-line coasts, providing a review of the methods that can be incorporated in such systems. Merrifield et al. [13] developed an EWS for wave-driven flooding, using regional wave and water-level observations, historical beach surveys, and a numerical runup model. This system provides the total water level by combining predictions of tides and sea-level anomalies with wave runup estimates. They stated that, as computing resources improve, real-time simulations could be incorporated into the EWS to reduce errors in the forecasts.

Despite the efforts that have been made to establish a framework for the development of an EWS, crucial steps must be taken to cover ground in the challenging issues of modelling nearshore hydraulics and simulating coastal inundation and drastically minimizing the required, intensive computations.

The short-term prediction of such events requires reliable open sea-state forecast data. Fortunately, in recent decades, technological achievements in computing and communications have propelled scientists into the information age, revolutionizing the manner in which they can acquire and utilize vast quantities of met-ocean data. Databases, providing open hindcast and forecast data, have become increasingly valuable commodities, enhancing scientists' arsenal for developing short-term forecast platforms. For instance, the authors of [14] presented an integrated modelling platform, designed to support the procedures of vessels approaching ports, which derives input data and boundary conditions from global- or regional-scale, open-sea and weather forecast databases, providing wave agitation in port basins and entrances. Nevertheless, the generation of a forecast platform in the operational environment is based on more than a state-of-the-art model. Such platforms implement daily applications of a number of high-resolution numerical models [15], e.g., a hydrodynamic model to simulate the storm surge, the nearshore currents and water levels, a spectral wave model to transfer wave characteristics from offshore to nearshore and a second wave model to simulate the wave field in the vicinity of the port. This procedure requires time-consuming processes and significant computational resources, along with the development and monitoring of a software architecture [16] for model coupling and integration. Apart from the aforementioned chain of numerical models, predicting coastal flood risk requires the implementation of additional numerical models to calculate nearshore hydraulics (e.g., wave overtopping) and simulate coastal inundation, further

increasing the computational burden and complexity of numerical models' cooperation, and thus prohibiting short-term forecasts. Hence, a cost-effective, yet accurate, way of predicting short-term coastal flood risks, with a forecast horizon ranging from a few hours to days, would be of paramount importance.

The ultimate goal of this study is to develop a reliable EWS to detect flooding potential and consequently improve societal preparedness for coastal flood risks. The methodological approach proposed herein involves the implementation and coupling of a suite of hindcast and forecast sea-state data, empirical formulas, high-credibility numerical (wave propagation and hydrodynamic) models and an Artificial Neural Network (ANN). The latter is a branch of Machine Learning (ML), a field of Artificial Intelligence (AI), used to induce regularities and patterns, providing easier implementation with low computational cost, as well as fast training, validation, testing, and evaluation, with high performance, and relatively less complexity. ANNs are chosen in the present study to predict the coastal flood risk and avoid the required implementation of time-consuming numerical models. In recent decades, ANNs have significantly contributed to the development of prediction systems and cost-effective solutions in the field of coastal engineering ([17–22]). The authors in [23] present the state-of-the-art of ML methods in inland flood prediction, providing an insight into the most suitable models and some guidelines for choosing the proper ML method.

The results of the proposed methodology should be in basic agreement with previous flooding patterns, and historical data should be used to evaluate these results. To this end, the study area of Rethymno in the Island of Crete, Greece, is examined herein to validate the proposed methodology. Most human activities in Rethymno are developed along its coastal front in the vicinity of the port. Major coastal flood events have been encountered throughout the years, mainly due to the combined effects of storm surge and wave overtopping, resulting in severe property and infrastructure damage and posing a serious threat to the safety of coastal residents.

The present paper is structured as follows: Section 2 describes the proposed methodological approach to developing an EWS and the frameworks of which it is composed; Section 3 describes a case study application; Section 4 discusses the results and provides directions for future research.

2. Methodological Approach for Developing a Coastal Flood EWS

The methodological approach we propose to develop an EWS consists of two frameworks, namely the "Hindcast Framework" (HF) and the "Forecast Framework" (FF). The scope of implementing an HF requires the creation of a suite of numerical models, validated against past flooding event patterns. Subsequently, the FF takes advantage of these validated models and runs a plethora of scenarios with distinct sea-state events (e.g., different sea water levels and wave characteristics) to train an ANN capable of predicting the impending coastal flood risks using offshore sea-sate data. Ultimately, the EWS will take as input offshore sea-state data from open databases and, by implementing the trained ANN, will provide coastal flood risk as output in a very short amount of time. The following subsections detail the aforementioned methodology and a flow chart is given in Figure 1.
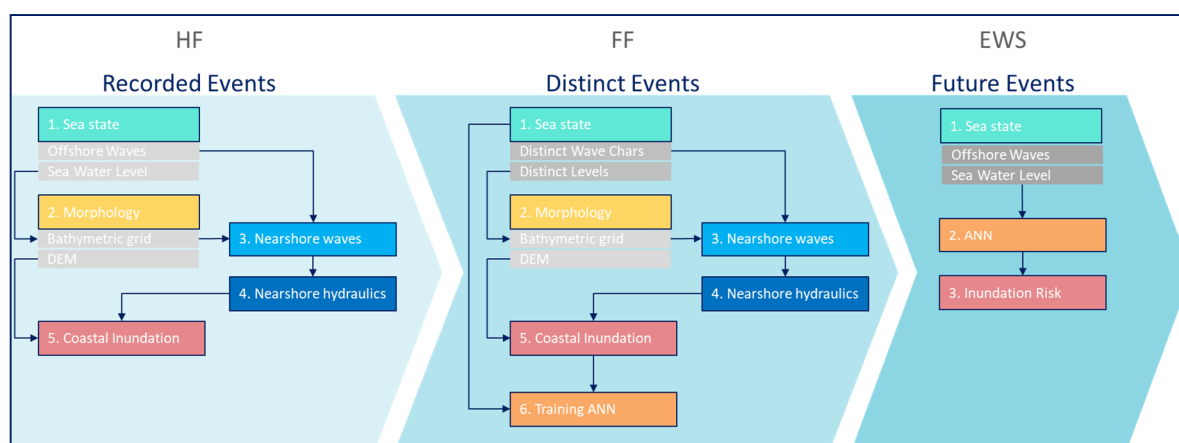
Figure 1. Flow chart of the proposed methodological approach to developing a coastal flood EWS and its frameworks (HF and FF).

2.1. Hindcast Framework (HF)

The scope of this framework is to identify past flood events and validate the implemented chain of numerical models and equations accordingly. The proposed HF is based on the work of [4], but is further enhanced herein to incorporate the utilization of open databases, the significant contribution of storm surge, and the implementation of a hydrodynamic model to simulate coastal inundation. Specifically, the HF consists of the following five steps:

1. Collecting sea-state hindcast data. The most crucial step of the entire process is identifying reliable sea state datasets during the occurrence of past coastal flood events. Valuable initiatives providing open data for metocean parameters have been developed and maintained in recent years. For instance, wave climate (significant wave height, peak period and mean wave direction) and storm surge elevation data can be obtained from Copernicus Marine Service [24]. Wave climate can also be distinguished in wind-waves and swell. Wind climate data can be obtained from National Oceanic and Atmospheric Administration [25]. Data regarding Astronomical Tide can be obtained from AVISO Satellite Altimetry Data [26];

2. Constructing a Digital Elevation Model (DEM) and a bathymetric grid based on executed hydrographic surveys, to represent the urban landscape and the sea bottom morphology of the study area, respectively;

3. Simulating nearshore wave field. Numerical simulations of wave transformation from offshore to nearshore should then be executed by implementing an appropriate wave model that accounts for all dominant phenomena taking place in the nearshore zone, i.e., shoaling, refraction, diffraction, depth-induced breaking and bottom friction;

4. Estimating profile nearshore hydraulics. The flood-prone study area is divided into subareas with a similar type of coastal front (e.g., sea walls, revetment, sandy or rocky beaches). Based on the simulated nearshore wave characteristics from the previous step, the wave setup, runup and overtopping can be calculated using empirical formulas or developed ANNs (e.g., [27,28]), in selected cross-shore transects along the flood-prone coastal front of each subarea. It is important to underline that the wave overtopping component is associated with high uncertainty, due to its non-linear, spatially and temporally variable stochastic nature. Incident wave characteristics and structural geometry significantly affect the overtopping process; therefore, attention should be paid on the assumptions being made. Factors incorporated into the overtopping calculation processes, such as friction and wave obliqueness coefficients, can be used as calibration parameters to validate overtopping discharge;

5. Simulating coastal inundation. The results of the previous step, along with the DEM, serve as input for simulating the inundation by implementing an appropriate hy-

drodynamic model, based on the shallow water equations, capable of describing the motion of water [29] in terms of depth-averaged, two-dimensional velocity and water depth in response to the forces of gravity and friction. Manning's coefficient, controlling the resistance to the flow, can be used as a calibration parameter to validate the spatiotemporal development of the flood.

2.2. Forecast Framework (FF)

The scope of the FF is to determine distinct sea-state events (wave height, period, direction and water level elevation) in relation to the wave climate and water-level variations in the study area, and subsequently run the respective nearshore wave, hydraulics and inundation simulations to identify the maximum flow depths and ultimately train an ANN for each subarea, with offshore sea-state characteristics as input, and target the maximum flow depths in each subarea of interest. Specifically, the FF consists of the following six steps:

1. Determining distinct sea-state events to be simulated. Given the orientation of the study area's shoreline and the wider geomorphology, the incoming wave directions to which the study area is exposed can be divided into 45-, 30- or 22.5-degree bins. Having acquired the wave climate data (from step 1 of HF) offshore the study area, an analysis is carried out to determine pairs of significant wave height, Hs (m), and peak wave period Tp (s) occurring from each direction. For each wave direction, distinct wave height values are determined with an equal incremental step, of 0.5 m or 1.0 m, starting from a threshold and reaching a maximum value. The threshold can be selected to describe rare events with only 10% of total wave heights (e.g., 2 m), thus defined as the 90th percentile of the dataset ([30]). It should be noted that the threshold can be more properly determined in relation to the geomorphology of the coastal front, e.g., by executing some preliminary overtopping calculations. The maximum value should be the maximum value that occurred in the available dataset, increased by a percentage to account for the higher wave heights that will occur in the near future and provide a wider range of results to train the ANN. Peak wave periods are determined with an equal incremental step of 1 s or 2 s, starting from a threshold (e.g., 5 s or 6 s) and reaching a maximum value (e.g., 15 s), which can be selected from the aforementioned analysis of wave heights and periods that were encountered in the dataset. Incident offshore wave climate can be further distinguished in swell and wind-waves according to the local conditions. Finally, Water Level (WL) elevations from Mean Water Level (MWL) are determined, with an equal incremental step of 0.5 m, 1.0 m or 2.0 m, starting from the Lowest Water Level (LWL) and reaching the Highest Water Level (HWL), which are known from step 1 of HF. The elevation between HWL and MWL can be further increased by a percentage to account for more intense future storm surge events. According to the selected distinct values of wave characteristics and water levels, specific offshore sea-state events are derived. Obviously, the more events there are (when selecting lower incremental steps) the better the ANN's training and efficacy. However, the selection of more events results in an increase in the computational effort required to simulate the respective physical processes. A balance should be maintained; therefore, it is preferable to meticulously define the threshold and maximum values for the abovementioned parameters rather than deriving a plethora of events within these bounds.
2. New bathymetric grids are produced, corresponding to each selected WL elevation from MWL. The results should be inspected to identify if the flood-prone area is "statically inundated" due to the water-level elevation, i.e., without wave action.
3. Numerical simulations of wave transformation from offshore to nearshore are then executed for each event, taking the corresponding bathymetric grid into account.
4. Based on the simulated nearshore wave characteristics from the previous step, the wave setup, runup and overtopping are calculated in a selected cross-shore transect along the flood-prone coastal front.

5. The results of the previous step serve as an input to simulate coastal inundation with a hydrodynamic model, and find the maximum flow depths in each subarea of interest.
6. Distinct sea-state event characteristics, i.e., offshore wave characteristics (height, period and mean wave direction) and water levels as defined in step 1, along with the corresponding maximum flow depths, as produced in step 5, are given as input for training an ANN. Additional randomly selected events are used for verification of the trained ANN.

2.3. Early-Warning System (EWS)

Given the trained ANN and the offshore sea-state forecasts that can be obtained from the open databases, an EWS can be established. The EWS takes the offshore wave characteristics and the sea water level elevation in relation to the MWL as input and, by implementing the ANN, it provides the maximum flow depth for each subarea as output. The corresponding inundation risk is determined by categorizing the resulted maximum flow depths into the following three categories:

1. Low Risk, indicating flow depths lower or equal than 0.15 m.
2. Medium Risk, indicating flow depths greater than 0.15 m and lower or equal to 0.35 m.
3. High Risk, indicating flow depths greater than 0.35 m.

It should be noted here that the above limits should not depend solely on the flow depths but also on flow velocities, the spatial extent of inundated areas and vulnerability of the coastal area. A combination of these parameters can yield a more comprehensive categorization of coastal flood risk. The limits adopted herein mainly rely on the national flood-risk mapping guidelines for the study area of Rethymno.

This tool can make predictions for future events, in a matter of seconds, with a forecast horizon that directly depends on the relevant horizon of the open databases, usually spanning from a period of hours up to seven days.

3. Implementation of the Proposed Methodology in the Flood-Prone Coastal Front of Rethymno

3.1. Study Area

The study area of Rethymno in the Island of Crete, Greece, in the Eastern Mediterranean Sea, was examined to validate the proposed methodology. The study area is located at the Prefecture of Rethymno, which is one of the four Prefectures of Crete. Rethymno city's population stands at 32,468 inhabitants, which characterize it as the third most populous urban area in Crete. The city is the center of the commercial, administrative and cultural activities of the homonymous Regional Unit, and most human activities are concentrated in the vicinity of the port area.

Major coastal flood events have been encountered throughout the years, mainly due to the combined effects of storm surge and wave overtopping, mostly over the revetment works of the parking area, as shown in Figure 2, resulting in severe damage and posing a serious threat to the safety of coastal residents. According to the visual observations of the residents, water can penetrate urban area in less than a half an hour from the initiation of the event (i.e., the first waves to overtop the revetment works of the parking and port areas), and its duration can reach a few hours. The frequent occurrence of these compound events emphasizes the need to establish an EWS.
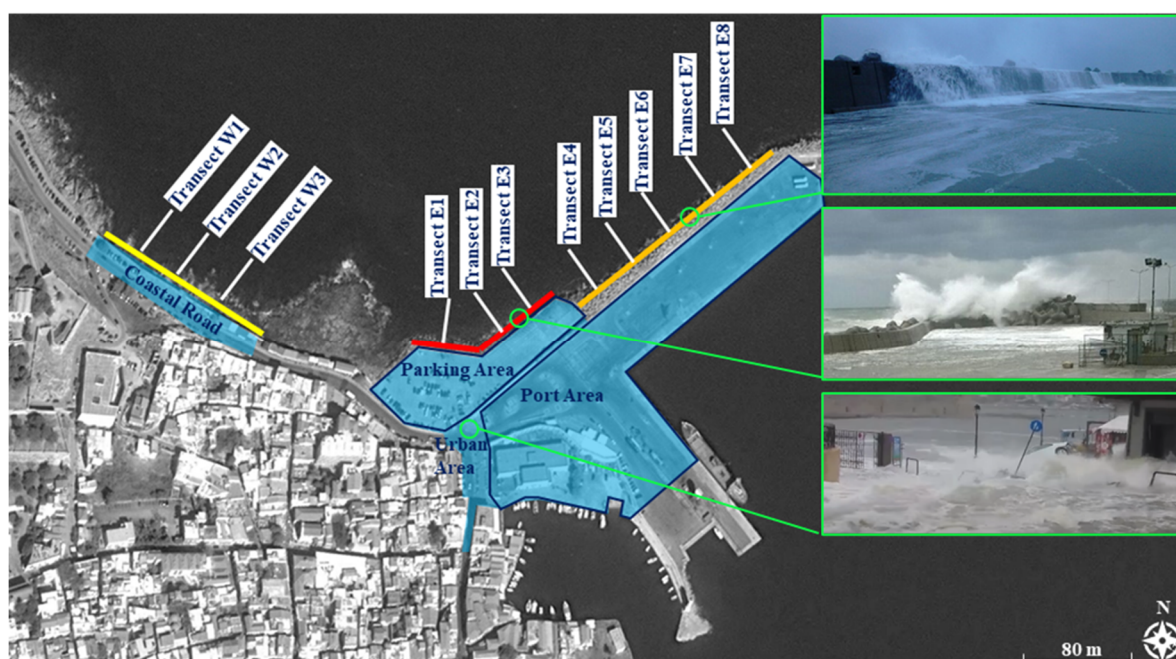
Figure 2. Flood-prone coastal areas of Rethymno. According to the observations, areas highlighted with a transparent light blue color (i.e., the coastal road west of the port, the parking lot, port and urban areas) are susceptible to being inundated by sea water during a storm. The sea–land interface boundaries, from which seawater can penetrate, are highlighted with yellow (in front of the coastal road), red (in front of the parking area) and orange (in front of the port's windward breakwater) lines. The eleven cross-shore transects (W1–W3 and E1–E8), where the nearshore hydraulic quantities were calculated, are depicted. Photographs illustrate wave overtopping and sea-water flowing over the land area.

3.2. Application of HF

Historical data were used to evaluate the results of the proposed framework. Therefore, four past coastal flooding events were considered due to the availability of video recordings of flood occurrence. The dates of these events are given in Table 1. During these events, sea-water-level elevation due to meteorological forcing (storm surge) and wave overtopping led to coastal inundation, posing serious threats to residents' safety. Based on video recordings of the events, the parking, urban and port areas (as defined in Figure 2) were heavily flooded, with significant flow depths and velocities, and overtopping was observed along the waterfront of the coastal road, west of the port.

Table 1. Sea-state data during past flood events in Rethymno, obtained from open databases.

Code Number of Storm Event		S1	S2	S3	S4
Date of Occurrence		11 December 2010	28 February 2012	1 January 2015	13 January 2015
Offshore Wave Char.	H_s (m)	5.24	5.19	4.98	5.79
	T_p (s)	9.23	9.23	9.23	10.15
	MWD (from North)	338.52°	356.9°	346.09°	358.77°
Elevation from MWL	Storm Surge (m)	0.15	0.30	0.26	0.23
	Astr. Tide (m)	0.03	0.02	0.02	0.01
	Total (m)	0.18	0.32	0.28	0.24

3.2.1. Collecting Sea State Hindcast Data

To obtain reliable sea-state data during these occurrences, open databases were used. Firstly, wave climate data were obtained from Copernicus Database, and specifically from

the package entitled MEDSEA_MULTIYEAR_WAV ([31]), for a period spanning from 1993 to 2019. This data package was produced by the Mediterranean Sea Waves forecasting system, which is a wave model based on WAM Cycle 4.5.4, developed as a nested sequence of two computational grids (coarse and fine) to ensure that swell propagating from the North Atlantic (NA) towards the strait of Gibraltar correctly enters the Mediterranean Sea (MED). The coarse grid covers the North Atlantic Ocean from 75° W to 10° E and from 70° N to 10° S in 1/6° resolution, while the nested fine grid covers the Mediterranean Sea from 18.125° W to 36.2917° E and from 30.1875° N to 45.9792° N with a 1/24° (~4.6 km) resolution. The Med-Waves modelling system resolves the prognostic part of the wave spectrum with 24 directional and 32 logarithmically distributed frequency bins. From this data package, wave characteristics were extracted at position 35.399849° N, 24.478480° E (at an approximate distance of 1.5 km seaward from port's windward breakwater), including the significant wave height, the peak period and the mean wave direction, on an hourly basis. Wave data were classified into equally spaced groups of wave heights, with a step of 1.0 m for each mean wave direction. The latter is the direction that the wave is coming from, measured clockwise from the North in degrees. Mean wave direction (MWD) is broken down into 30-degree bins, i.e., 12 sectors (N, NNE, ENE, E, ESE, SSE, S, SSW, WSW, W, WNW and NNW). To visualize the frequency and height of waves by direction, a rose diagram is illustrated in Figure 3. The radial length of each bin in the rose diagram represents the frequency, and the distribution of colors on each bar represents the wave height groups corresponding to the legend. It is apparent from Figure 3 that the most frequent incident direction, which significantly affects the study area, with the highest occurring wave heights reaching the wave group of 6.0–6.5 m, is the North, as was anticipated due to the larger fetch lengths (>120 km) and wind climate characteristics. The maximum wave height occurred (on 10 February 2015) equals to 6.37 m, with a corresponding period of 10.15 s, coming from 351.39° N. Unfortunately, there are no video recordings of this storm; therefore, it is not further considered herein.
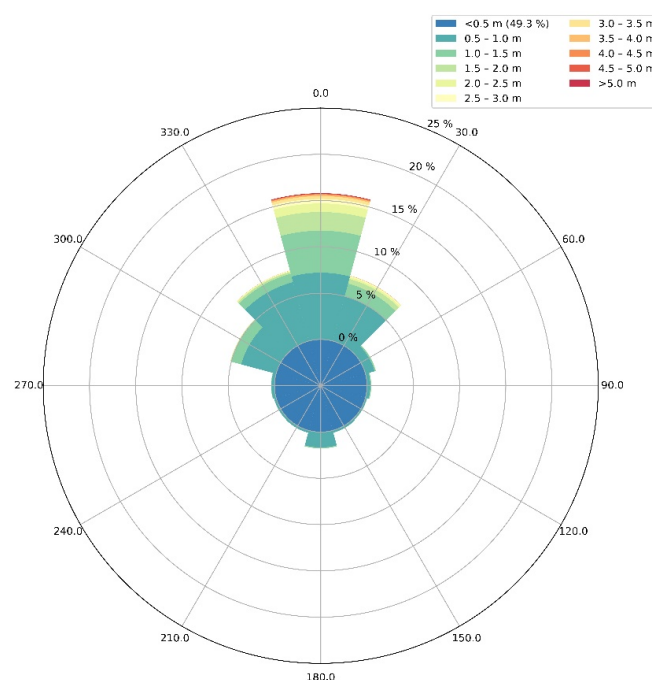
Figure 3. Wave Rose Diagram of Mean Annual Significant Wave Heights, H_s (m), offshore of the Rethymno area.

Storm surge elevation data were also obtained from the same database, specifically from the package entitled MEDSEA_MULTIYEAR_PHY_006_004 ([32]), for a period span-

ning from 1987 to 2019, at hourly intervals. The highest water-level elevation that occurred in this dataset was approximately +0.40 m, and the lowest −0.50 m from MWL.

Finally, data regarding Astronomical Tide (from 1983 to 2017 at hourly intervals) were obtained from AVISO Satellite Altimetry Data ([26]), and specifically from its product named FES 2014b. FES2014 is the last version of the Finite-Element Solution (FES) global tide model provided by AVISO. It takes advantage of longer altimeter time series and better altimeter standards, improved modelling and data assimilation techniques, a more accurate ocean bathymetry and a refined mesh in most shallow-water regions. Computations are performed in a global finite-element grid (~2.9 million nodes), providing the geocentric (elastic) tide at each computational node. Model outputs concern 34 tidal constituents, distributed on a 1/16° grid. According to this dataset, MWL was 0.0 m, Highest Astronomical Tide (HAT) was +0.05 m, Mean High Water (MHW) was +0.02 m, Mean Low Water (MLW) was −0.02 m, Lowest Astronomical Tide (LAT) was −0.05 m, and the mean tidal range was 0.04 m. It is observed that the astronomical tide has a low range, and thus made a minor contribution as a flood-driver, while storm surge played the dominant role in sea-water elevation. The aforementioned sea-state datasets have been extensively documented and validated and were found to be homogenous, without the presence of faulty or unrealistic data for the particular area of interest. Sea-state data for each past coastal flood event at the time of video recordings are given in Table 1. It is observed that, according to the data obtained from the databases, high-energy waves, with heights equal to or greater than 5 m, were present offshore the study area at the same time that coastal inundation was taking place, according to the video recordings, indicating that the predictions of these databases were close to reality.

3.2.2. DEM and Bathymetric Grid

Additionally, a DEM was available from a relevant previous project, entitled "Pearl-Preparing for extreme and rare events in coastal regions" ([33]), for the study area, with a fine spatial resolution of 0.8 m in both horizontal dimensions. A bathymetric grid was also constructed, based on executed hydrographic surveys with a spatial step of 2.5 m.

3.2.3. Simulating Nearshore Wave Field

Numerical simulations of irregular wave transformation from offshore to nearshore were then executed by implementing a nonlinear mild-slope wave model of parabolic approximation, developed by [34], based on the work of [35], which derived a parabolic equation governing the complex amplitude, A, of the fundamental frequency component of a Stokes wave. Publication [36] improved the parabolic equation and its validity range by developing approximations based on minimax principles to allow for large-angle propagation. The range of allowable wave angles within the limitations of the parabolic approximation was significantly increased by relaxing the local accuracy of approximations based on Padé approximants at normal wave incidence in favour of minimax approximations, which minimize the maximum error that occurs over a prespecified range of wave directions. The revised governing parabolic equation, allowing for the study of waves with larger wave incidence angles with respect to the x axis (the principal direction of propagation), is given by:

$$C_g A_x + i\left(\bar{k} - a_0 k\right) C_g A + \tfrac{1}{2}\left(C_g\right)_x A + \tfrac{i}{\omega}\left(\alpha_1 - b_1 \tfrac{\bar{k}}{k}\right)\left(CC_g A_y\right)_y - \tfrac{b_1}{\omega k}\left(CC_g A_y\right)_{yx} + \tfrac{b_1}{\omega}\left(\tfrac{k_x}{k^2} + \tfrac{(C_g)_x}{2kC_g}\right)\left(CC_g A_y\right)_y +$$

$$\tfrac{i\omega k^2}{2} D|A|^2 A + \tfrac{w}{2} A = 0 \qquad (1)$$

where the parameter D is given by $D = \dfrac{\left(cosh4kh + 8 - 2tanh^2 kh\right)}{8sinh^4 kh}$, the complex amplitude A is related to the water surface displacement by $\eta = Ae^{-i(kx - \omega t)}$, k the local wave number related to the angular frequency of the waves, ω, and the water depth, h. Parameter $\bar{k}$ is a reference wave number, taken as the average wave number along the y axis, C is the phase celerity, C_g is the group celerity and w is a dissipation factor accounting for depth-induced

breaking and bottom friction. Finally, coefficients a_0, α_1 and b_1 depend on the aperture width chosen to specify the minimax approximation [37].

The model allows for the generation and propagation of monodirectional irregular waves by dividing the wave energy spectrum into discrete wave components and performing separate simulations for each one. The significant wave height, Hs, is then obtained at each cell of the computational domain by linear superposition of the discrete wave components. The spectrum is divided into bands of equal wave energy using either a JONSWAP or TMA spectrum source function, ensuring that each discrete wave component has the same fraction of wave energy and, hence, the same wave height. Implementing this discretization method ensures the accuracy of the results while avoiding the specification of a high number of discrete wave components, which are usually required by the single summation methods utilized to discretize the wave-energy spectrum [38].

The spatial distribution of nearshore wave heights corresponding to the first event is illustrated in s retained the largest proportion of their offshore energy when attacking the flood-prone coastal front, in contrast to the adjacent shores, where a wide breaker zone occurs, and waves reach the shoreline with significant energy loss. This can be attributed to the local foreshore morphology, where steep sea-bottom slopes are present in front of the flood-prone areas (Figure 4).
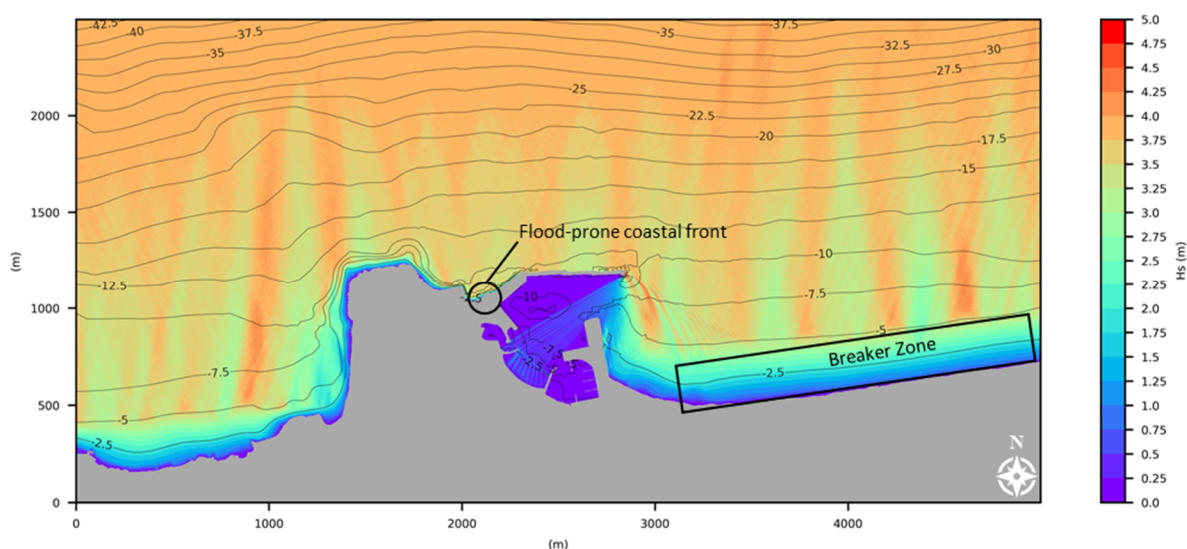
Figure 4. Simulation results of spatial distribution of nearshore wave heights (indicated by color palette) for the flood event in 10 December 2010; contours indicate sea water depths.

3.2.4. Estimating Profile Nearshore Hydraulics

Having determined the nearshore wave field, the flood-prone study area was then divided into subareas with a similar type of coastal front. As shown in Figure 2, the first subarea is the "coastal road" with a seawall in front of it, the second is the "parking area", the third is the "urban area" landward of the parking area, and the last one is the "port area". Rubble mound structures were constructed in the front of the parking area and the port's windward breakwater. Eleven transects were selected along the solid boundaries of these areas, i.e., W1–W3 and E1–E8. The wave overtopping discharges were calculated in these transects.

The front boundary of the coastal road of Rethymno (Figure 2) consists of a composite seawall, i.e., an almost vertical wall fronted by natural rock mound, which significantly affects wave-breaking conditions but remains below water level during the storm, along with an influencing foreshore. The front boundaries of the parking area and the port's windward breakwater consist of steeply sloping rubble mound structures with armor layers of concrete units (Tetrapods). The average overtopping discharge, q (l/s/m), is estimated through the Neural Network developed by [39,40], as presented in [28]. In the present

study, this Neural Network was implemented in the front boundaries of the parking area and the port's windward breakwater to calculate overtopping discharge, since it accounts for more structural parameters than the empirical formulas of [28], and thus yields more accurate predictions. Representative results are given in Table 2 for characteristic transects along the coastal front. It can be observed that the largest overtopping volumes occurred in transect E2, which is in front of the parking area. Indeed, according to the visual observations of the residents, the urban area was mainly inundated from sea-water penetrating this boundary.

Table 2. Simulated wave heights at the toe of the structures and corresponding mean wave overtopping discharges.

	Transect	S1	S2	S3	S4
	W2	3.42	3.85	3.53	4.31
Wave Height at structure's toe H_{m0} (m)	E2	4.15	4.31	4.16	4.45
	E5	5.48	4.93	5.03	5.33
	W2	1.00	2.14	1.15	6.92
Overtopping discharge q (l/s/m)	E2	34.90	53.30	41.70	58.90
	E5	7.85	1.82	2.68	8.09

3.2.5. Simulating Coastal Inundation

The calculated overtopping discharges along the boundaries and the DEM serve as input for the inundation simulation by implementing the hydrodynamic model HEC-RAS 2D (US Army Corps of Engineers, Davis, CA, USA, 2016), which is the last step of the proposed model suite of HF. HEC-RAS 2D solves the shallow-water equations (SWE), which describe the motion of water in terms of depth-averaged 2D velocity and water depth in response to the forces of gravity and friction. These equations represent the conservation of mass and momentum in a plane [29]). The water can move to any direction based on the given topography and resistance to the flow controlled by the land-use type and associated Manning's coefficient [41]. The model area is discretized into grid cells, where each cell uses the underlying terrain data with less loss of resolution (sub grid model). The continuity and momentum equations are expressed as follows [42]:

$$\frac{\partial \zeta}{\partial t} + \frac{\partial p}{\partial x} + \frac{\partial q}{\partial y} = 0 \tag{2}$$

$$\frac{\partial u}{\partial t} + v\frac{\partial u}{\partial x} + u\frac{\partial u}{\partial y} = -g\frac{\partial H}{\partial x} + v_t(\frac{\partial^2 u}{\partial x^2} + \frac{\partial^2 u}{\partial y^2}) - c_f u + fu \tag{3}$$

$$\frac{\partial v}{\partial t} + u\frac{\partial v}{\partial x} + v\frac{\partial v}{\partial y} = -g\frac{\partial H}{\partial x} + v_t(\frac{\partial^2 v}{\partial x^2} + \frac{\partial^2 v}{\partial y^2}) - c_f v + fv \tag{4}$$

where u and v are the velocities in the Cartesian directions; g is the gravitational acceleration; v_t is the horizontal eddy viscosity coefficient; c_f is the bottom friction coefficient and f is the Coriolis parameter. When the diffusive wave is selected, the inertial terms of the momentum equations (Equations (3) and (4)) are neglected.

The generated computational grid of the area of interest comprises about 235,000 cells, resulting in an average cell size of 1.00 m^2 (i.e., DEM spatial resolution 1 m). The simulation time is set as 1 h. The computation settings of the unsteady flow analysis are performed using a computational interval equal to 1 s and mapping output interval equal to 1 s. The hydrograph output interval is set as 1 min and the detailed output interval is also set as 1 min. The full momentum method used to compute unsteady flow field was used, due to the higher accuracy achieved compared to the diffusion wave method, and the maximum iterations were equal to 10. However, the maximum number of iterations

during calculations was 2. All other parameters and unsteady computation options and tolerances are set as default from the HEC-RAS 2D.

One of the most important factors in flood inundation modelling in built-up areas is the building representation within the 2D hydraulic–hydrodynamic model. The building representation method used in this research assumes that each cell of the mesh/grid that is located inside a building block area is represented by a local increase in elevation. Thus, each building block is modified in the DEM to have more elevation than the bare-earth altitude.

The Manning's roughness coefficient was estimated using the proposed land-cover classification in combination with typical Manning's roughness coefficient tables. Manning's coefficient was used as a calibration parameter and set as 0.02 m$^{-1/3}$/s in the entire computational area to capture the spatiotemporal development of the flood, given that water penetrated the urban area in less than a half an hour from the initiation of the event, according to the visual observations of the residents. The maximum inundated area stemming from video recordings and local stakeholders' observations during past flood events is given in Figure 5, while inundated areas resulting from the one-hour simulations for each past storm event considered (i.e., S1–S4) are depicted in Figure 6. The results satisfactorily capture the spatial extend of the inundation. Nevertheless, it should be noted that the observed inundated areas rely on video recordings of the time that events occurred and observations of local stakeholders, not on field measurements.

Figure 5. Maximum inundated area (highlighted with red color) from video recordings and local stakeholder observations.
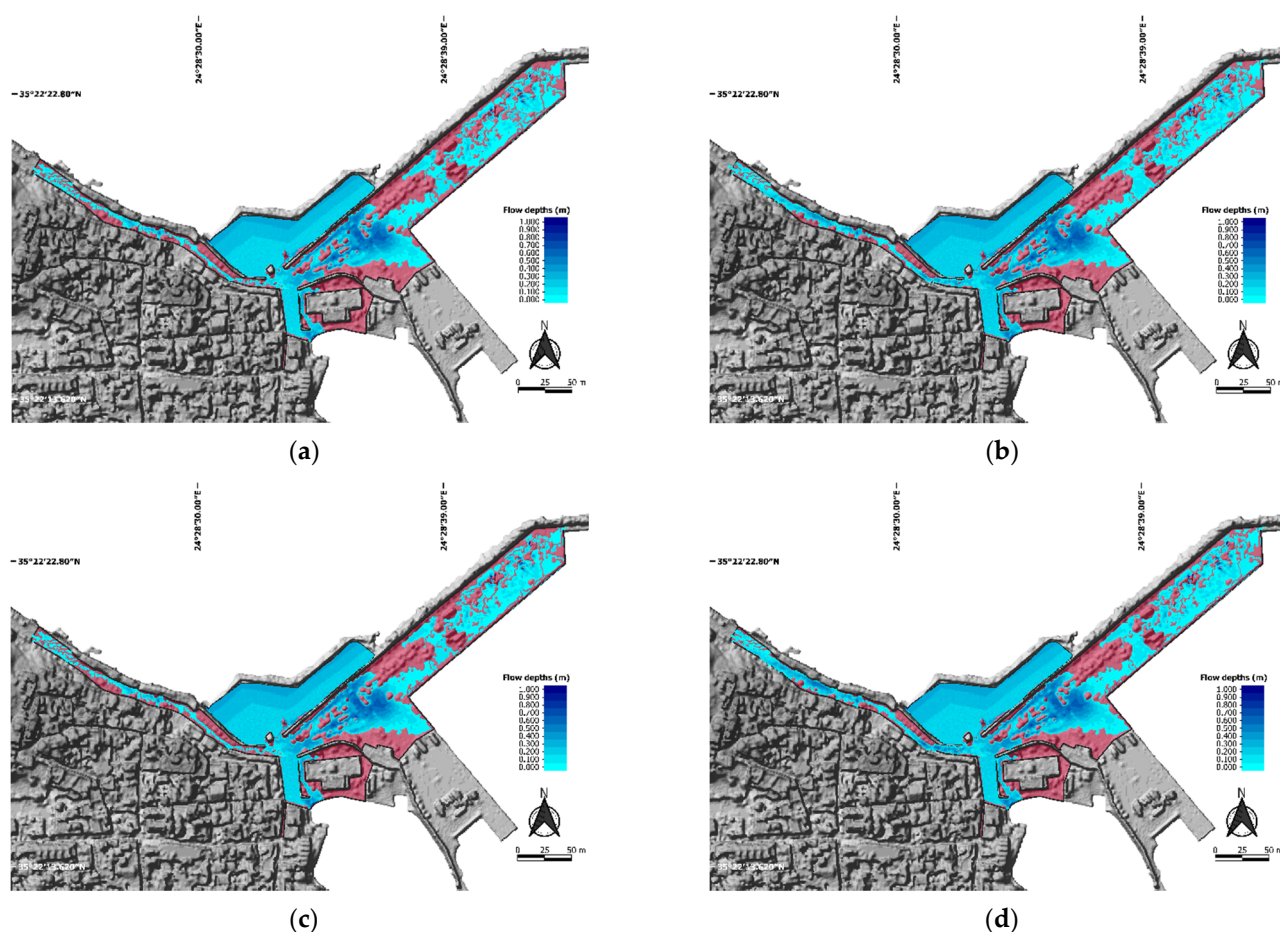
Figure 6. Inundated areas according to simulation results (highlighted with blue color palette) for storm events: (**a**) S1, (**b**) S2, (**c**) S3 and (**d**) S4 on top of the maximum inundated area from video recordings and local stakeholders' observations (highlighted with red color).

3.3. Application of FF

It can easily be deduced that an infinite number of sea-state events can occur in future. To train an ANN that is capable of predicting the respective coastal flood risk, a sufficient number of distinct sea-state events should be considered. Given the orientation of the study area's shoreline and the wider geomorphology, the incoming wave directions to which the study area is exposed are divided into 30-degree bins, providing sufficient accuracy given that waves generated from the N sector generally dominate the wave climate. Having acquired the wave climate data (from step 1 of HF) offshore of the study area, an analysis was carried out to determine pairs of significant wave height, H_s (m), and peak wave period, T_p (s), occurring in each direction (WNW, NNW, N and NNE), as follows.

In Figure 7, pairs of significant wave heights equal to or greater than 2 m, and peak wave periods equal to or greater than 6 s, from the available dataset for each direction, are illustrated with blue dots. It is observed that waves with heights equal to 2 m occurred, with peak periods ranging from approximately 6 s to 13 s; waves with heights equal to 3 m occurred, with peak periods ranging from approximately 6 s to 12 s; waves with heights equal to 4 m occurred, with peak periods ranging from approximately 7 s to 12 s; waves with heights equal to 5 m occurred, with peak periods ranging from approximately 8 s to 11 s; and finally, waves with heights equal to 6 m occurred, with peak periods ranging from approximately 9 s to 11 s.
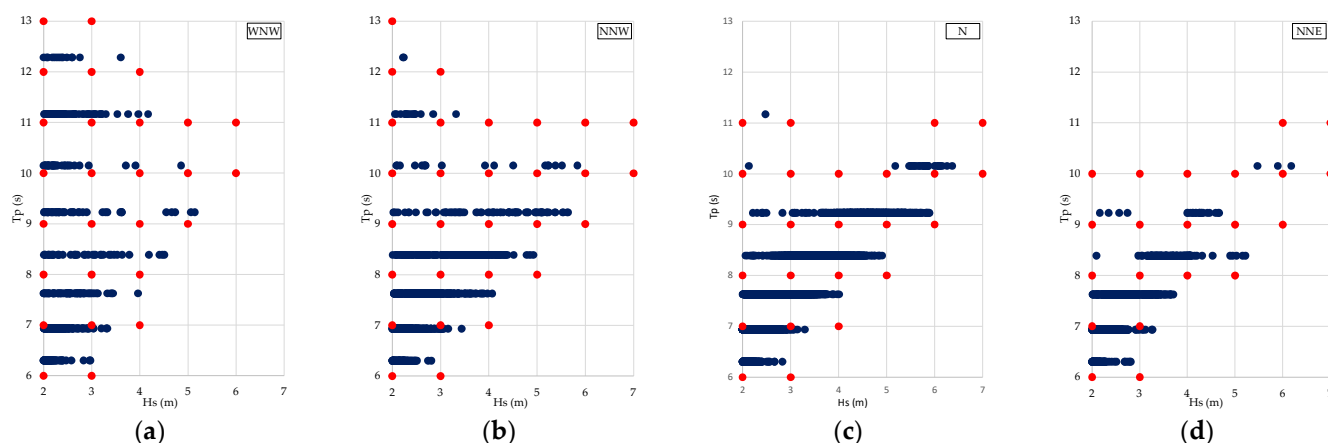
Figure 7. Pairs of offshore wave heights and peak periods from the available dataset (blue dots) and selected pairs (red dots) for training the ANN; (**a**) WNW direction, (**b**) NNW direction, (**c**) N direction and (**d**) NNE direction.

In light of the above distribution of pairs for each of these wave directions, specific wave height values are determined to form the training dataset for the ANN, with a constant incremental step of 1.0 m starting from a threshold and reaching a maximum value. The significant wave height threshold was set as 2 m while the maximum value was set as 7 m (greater than the maximum one that occurred in the available dataset, i.e., 6.37 m). Peak wave periods were also chosen, with a constant incremental step of 1s, starting from a threshold of 6 s and reaching a maximum value of 13 s. Additionally, Water Level (WL) elevations were prescribed, with a constant incremental step of 0.5 m, resulting in three levels: Lowest Water Level (LWL), which is equal to −0.5 m from MWL, MWL, and Highest Water Level (HWL), which is equal to +0.5 m from MWL.

The HWL considered for training the ANN was deliberately chosen as higher than the maximum one occurred in the available hindcast dataset, i.e., +0.40 m from MWL as previously mentioned, to account for a mean sea-level rise due to climate change in the coming years and/or the occurrence of more intense storms, temporarily leading to an even higher rise in sea-water level. Hence, an assumption of an additional 10 cm that may occur due to a mean sea-level rise, a storm (more intense than the maximum occurred in recent years) or a combination of these two parameters, was made herein. This assumption can be considered reasonable given the following. In general, the lifecycle of the coastal flood early-warning system is expected to reach up to ten years. Beyond this period, it is very likely that the nearshore geomorphological conditions will change (e.g., due to erosion of the coastal front) or coastal protection works be constructed, affecting the wave overtopping process. According to the recently published Ocean State Report 5 from the Copernicus Marine Service and Mercator Ocean International [43] the trend of mean sea level rise of the Mediterranean Sea (where Rethymno is located), from 1993 to 2020, was +0.25 (±0.083) cm/yr. By conservatively adopting the upper limit of this trend (i.e., +0.33 cm/yr) the mean sea level, in the coastal front of Rethymno, will rise by 3.33 cm in ten years. Consequently, noting the HWL (i.e., +0.50 m from MWL) used to train the ANN, the remaining 46.67 cm could account for a sea-water level rise due to a more intense storm. This value is, again, larger than the maximum one observed in the available hindcast dataset (i.e., 0.40 m), by almost +17%.

In a similar manner, to incorporate climate change's impact on offshore wave climate, which could lead to greater wave characteristics, the upper limits of the wave characteristics used to train the ANN are deliberately made higher than the maximum ones that occurred in the available hindcast dataset. The maximum significant wave height that is considered is equal to 7 m, and the maximum considered peak period is equal to 13 s, while the maximum significant wave height that occurred was 6.37 m and the maximum peak period was 12.28 s.

The ANN, with a training process based on a range of water levels, (LWL, MWL and HWL) and a variety of offshore wave pairs, will be able to provide results that are

reasonably beyond the considered upper limits. According to the selected distinct values of wave characteristics (red dots in Figure 7) and the three water levels, 303 specific sea-state events were derived.

Subsequently, new bathymetric grids were produced, corresponding to each water level, and numerical simulations of wave transformation from offshore to nearshore were carried out by implementing the aforementioned wave model. Extracting the wave characteristics at the toe of the coastal structures and the water level, the mean wave overtopping discharges were calculated by applying the Neural Network ([39,40]), as presented in [28], in the eleven selected cross-shore transects along the flood-prone coastal front of each subarea of interest. The results of the wave overtopping, extracted at three transects (E5, E2 and W2), are shown in Figure 8 for each of the 303 selected sea-state events. This figure is revealing. Firstly, it can be seen that waves from the NNW and N directions caused greater wave overtopping, followed by waves from the WNW and the NNE directions. As expected, the elevated WLs (i.e., MWL and HWL) resulted in more severe wave overtopping in comparison to the LWL for the same offshore wave characteristics. Furthermore, it can be observed that the largest overtopping volumes occurred in transect E2 (in comparison to E5 and W2), which is in front of the parking area, coinciding with the visual observations of the residents.
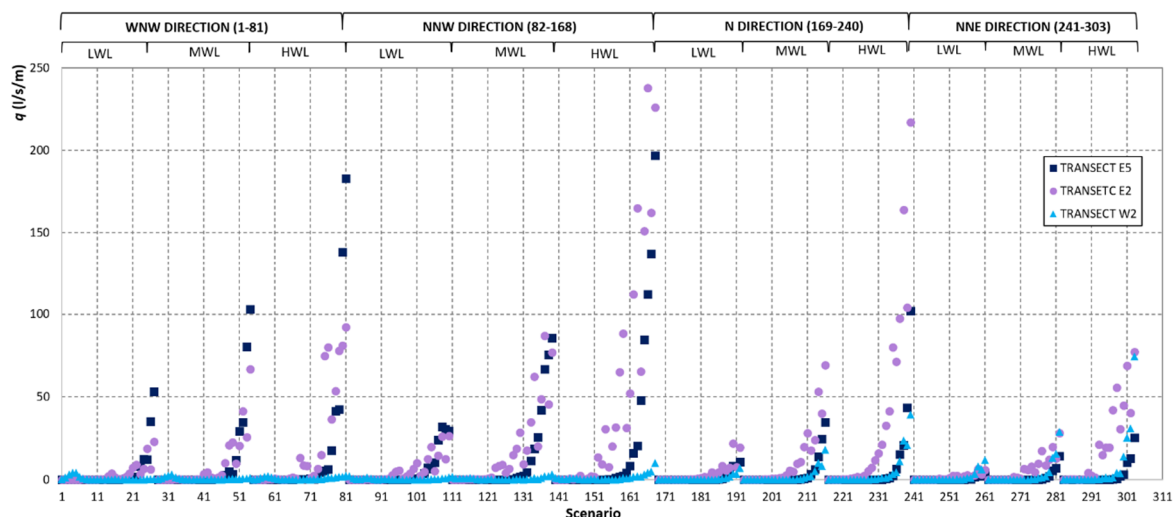
Figure 8. Wave overtopping in three transects E5 (dark blue squares), E2 (purple dots) and W2 (light blue triangles) for 303 selected sea state events.

The results of the previous step set the stage for the next step of simulating coastal inundation with the aforementioned hydrodynamic model to find the maximum flow depths for each subarea. The coastal flood risk was then classified into the three categories of low-, medium- and high-risk level (as mentioned in the last paragraph of the previous chapter), for each of the 303 sea-state events. In Figure 9, the coastal flood-risk categorization in relation to selected offshore wave characteristics, i.e., H_s, T_p, for each direction of interest (WNW, NNW, N and NNE) and for LWL and HWL, are depicted for the most vulnerable subarea, i.e., the parking area. It is observed that medium- and high-risk levels are caused by offshore wave heights equal to or greater than 3 m and peak wave periods equal to or greater than 7 s, except in one case of the NNW direction, in which a wave height of 2 m and peak period of 13 s caused a medium-risk level. Akin to wave overtopping, waves coming from the NNW and N directions were responsible for generating the highest number of high-risk level events. In addition, noting that the mean annual frequency of occurrence of wave heights equal to or greater than 3 m was 1.245% for the N direction, 0.114% for the NNW, 0.098% for the NNE and 0.026% for the WNW, it can be argued that the N direction causes the most coastal floods in the area of Rethymno. Furthermore, it can be seen from

Figure 9 that the elevated WLs (e.g., HWL) substantially increase the risk in comparison with the LWL, proving that storm surge plays a crucial role as a driver of floods.
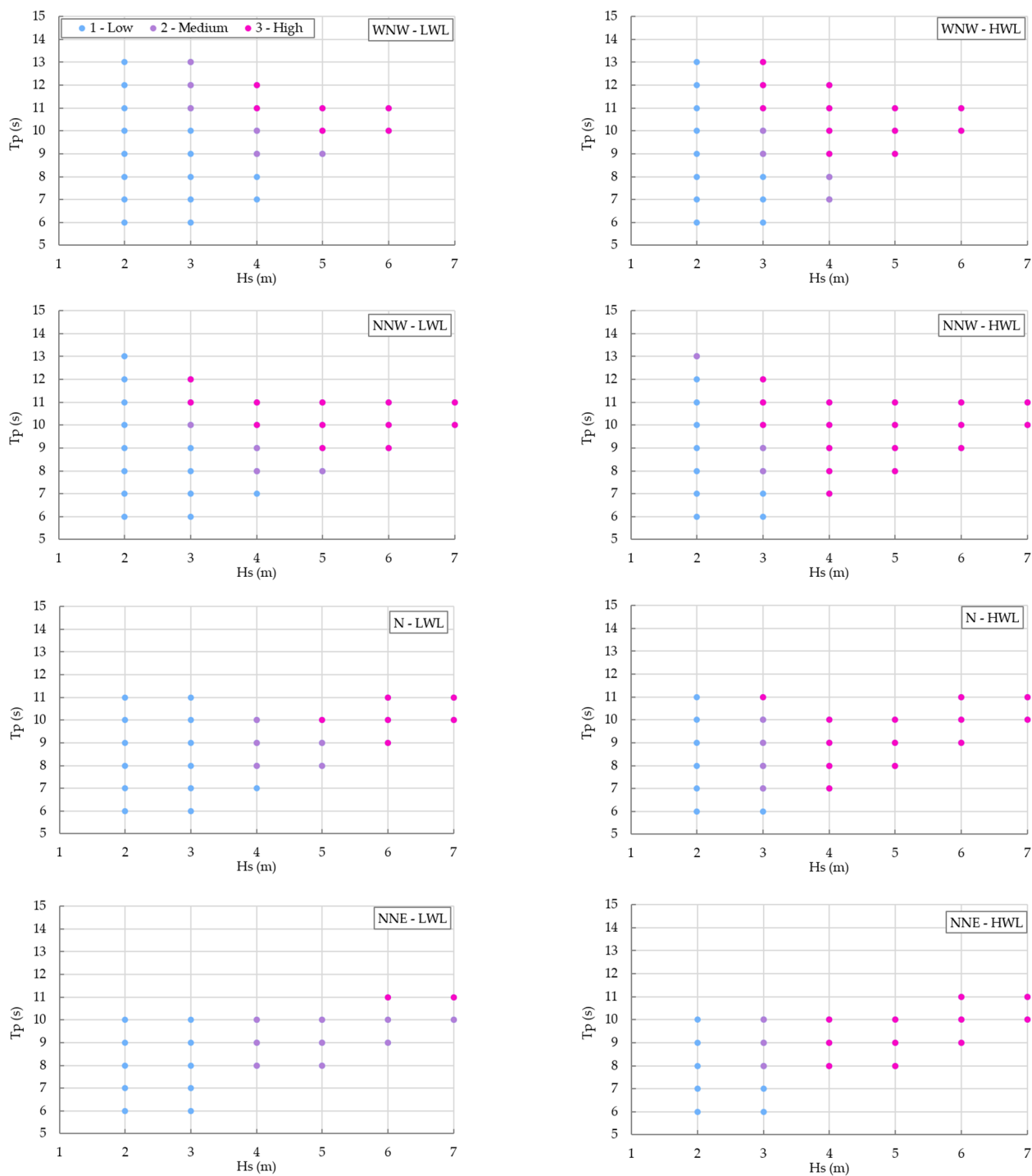
Figure 9. Coastal flood-risk levels in relation to offshore wave characteristics of selected distinct events, i.e., H_s, T_p and direction (WNW, NNW, N and NNE) and sea-water levels, i.e., LWL (**left panel**) and HWL (**right panel**), for the parking area. Light blue dots represent a low-risk level, purple represent a medium-risk level and pink represent a high-risk level.

Having related the sea-state data with respective flood-risk levels, an ANN can be constructed and implemented. Three datasets are needed to train an ANN, namely, the training dataset, the validation dataset (to measure the generalisation capability) and the test dataset. Training and validation sets compose the generalisation set, which contains

the necessary data for developing an ANN, while the test dataset does not participate in the training process and is used as an independent measure of the performance of the developed ANN. In the present study, the generalisation dataset consisted of the data of the 303 events, as presented above, which were divided into 273 events for the training dataset and 30 randomly selected events for the validation dataset. Finally, the test dataset consisted of 22 additional randomly selected events, as will be presented later.

Multilayer feed-forward ANNs are used to predict the coastal flood risk under varying combinations of offshore sea-state conditions (wave characteristics and sea water levels). A variety of ANN architectures were developed in the context of this framework. The ANNs implemented herein were composed of three or four layers, with the first one being the input layer sending data to the network, the second one the hidden (single or double) layer to generate results based on the input, and the third one the output layer to provide the results. The number of neurons and hidden layers composing the ANN architecture is paramount to its performance. In general, fewer neurons and hidden layers will result in low accuracy, while too many neurons and hidden layers will increase complexity. The most commonly employed methods to determine the number of hidden neurons are experimentation and trial and error.

The four input parameters (p) used for the input layer are the offshore significant wave height, H_s^{in}, peak period, T_p^{in}, mean wave direction, MWD^{in}, and the water level, WL^{in} (i.e., LWL, MWL and HWL). The target output parameters (d) used for the output layer are the maximum flow depths in each subarea of interest (Figure 2), i.e., the port area, d_{port}^{in}, the parking area, d_{park}^{in}, the urban area, d_{urbn}^{in}, and the coastal road, d_{road}^{in}. Input and output parameters are normalized such that they always fall within a specified range [0,1] to eliminate errors associated with the characteristics and magnitudes of the data. The normalized values were obtained via the minmax method as:

$$p_i^n = \frac{p_i - P_{min}}{P_{max} - P_{min}} \tag{5}$$

where p is the input/output parameter, i is the number of the dataset event, superscript n indicates the normalized parameter, and P_{min} and P_{max} are the minimum and the maximum values of the parameters in the entire dataset, respectively.

The normalized values of the input parameters propagate from the input layer (In) through the hidden layers ($HL1$, $HL2$) to the output layer (out). The output is calculated as follows:

$$x_j^{HL1} = F\left[\left(\sum_{i=1}^{N1} w_{ij}^{HL1} x_i^{In}\right) - \theta_j^{HL1}\right] \quad j = 1, \dots, N1 \tag{6}$$

$$x_j^{HL2} = F\left[\left(\sum_{i=1}^{N2} w_{ij}^{HL2} x_i^{HL1}\right) - \theta_j^{HL2}\right] \quad j = 1, \dots, N2 \tag{7}$$

$$\left(x_j^{out}\right)^n = F\left[\left(\sum_{i=1}^{4} w_{ij}^{out} x_i^{HL2}\right) - \theta_j^{out}\right] \quad j = 1, \dots, 4 \tag{8}$$

where $N1$ and $N2$ are the number of neurons in the hidden layers $HL1$ and $HL2$; w_{ij} are numerical weights (between the input and hidden layers w_{ij}^{HL1}, w_{ij}^{HL2}); θ_j are the biases, and F is the transfer function.

The hyperbolic tangent sigmoid function was applied to the hidden layers to describe the nonlinear relationship:

$$f(x) = \frac{2}{1 + e^{-2x}} - 1 \tag{9}$$

In the output layer, a linear transfer function, $f(x) = x$, is used.

In this study, the initial weighting values and biases were randomly assigned and the ANN is trained using the dataset to assign the optimum weights and biases. The

Mean Squared Error (MSE) between the predicted parameters by the generalization set and the output target parameters was used to determine the optimum architecture as follows:

$$\text{MSE} = \frac{1}{N} \sum_{i=1}^{N} \left[\left(x_j^{out} \right)^n - \left(x_j^{target} \right)^n \right]^2 \tag{10}$$

where N is the number of generalisation set samples (i.e., 303 in the present work). The MSE was utilized to adjust weights and biases using the gradient descent method:

$$w'_{ij} = w_{ij} - \kappa \frac{\partial \text{MSE}}{\partial w_{ij}} \tag{11}$$

$$\theta'_{ij} = \theta_{ij} - \kappa \frac{\partial \text{MSE}}{\partial \theta_{ij}} \tag{12}$$

where w'_{ij} and θ'_{ij} are the updated weights and biases after each iteration and κ is the learning rate. The maximum number of iterations was set to 1000 and the acceptable MSE was lower than 0.003.

As mentioned above, a variety of ANN architectures were developed and compared to determine the optimum numbers of hidden layers and neurons. Single and double hidden layers (Figure 10) were considered, with the following architectures: {4-4-4}, {4-8-4}, ... , {4-32-4} and {4-6-6-4}, {4-8-8-4}, ... , {4-16-16-4}.
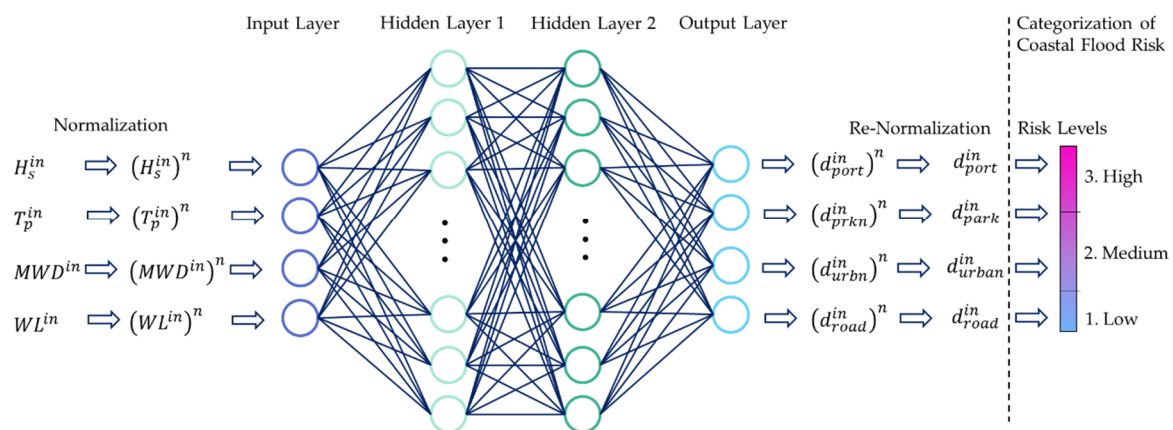

Figure 10. ANN architectures tested to predict the coastal flood risk.

For these architectures, the MSE and the correlation factor, R, were calculated and are presented in Figure 11a,b, respectively, to assess the performance of each configuration. It is observed that the double hidden layer produced an overall lower MSE and greater R in contrast with a single hidden layer and is, therefore, preferable. The architecture {4-12-12-4} was adopted as the optimum one since it produces the minimum MSE, equal to 0.0003, with the highest correlation factor, R, equal to 0.995. The ANN-predicted values for the respective targets of the generalisation dataset are presented in Figure 12a.

To test the performance of the developed ANN, an additional dataset is provided to compare the ANN predictions with the respective targets. This test dataset consists of 22 additional events, as shown in Table 3. The four previous flooding events (TS1–TS4), as presented in the HF application, were included to assess the performance of the ANN, along with 18 randomly selected events. The latter consist of randomly selected sea-state conditions with offshore wave heights ranging from 2.05 m to 6.73 m, peak periods ranging from 6.05 s to 10.87 s, an MWD ranging from WNW to NNE, and a WL ranging from −0.49 m to +0.40 m (from MWL). Steps 2–6 of the FF were applied to derive the coastal flood categorization for each of these events.
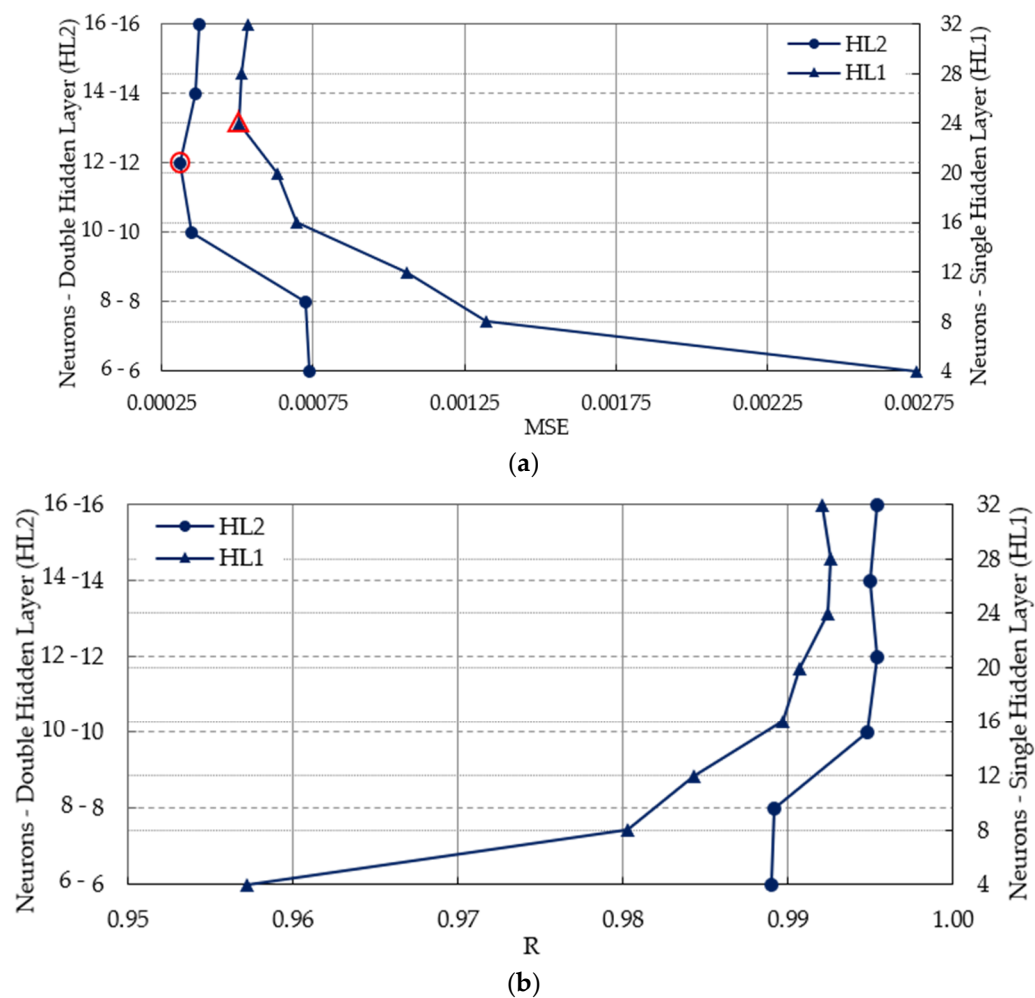
Figure 11. (**a**) Mean squared errors, MSE, and (**b**) correlation factors, *R*, for the considered ANN architectures of single (triangles), HL1, and double (dots), HL2, hidden layers and various numbers of neurons. The minimum MSE is outlined with red for each hidden layer.
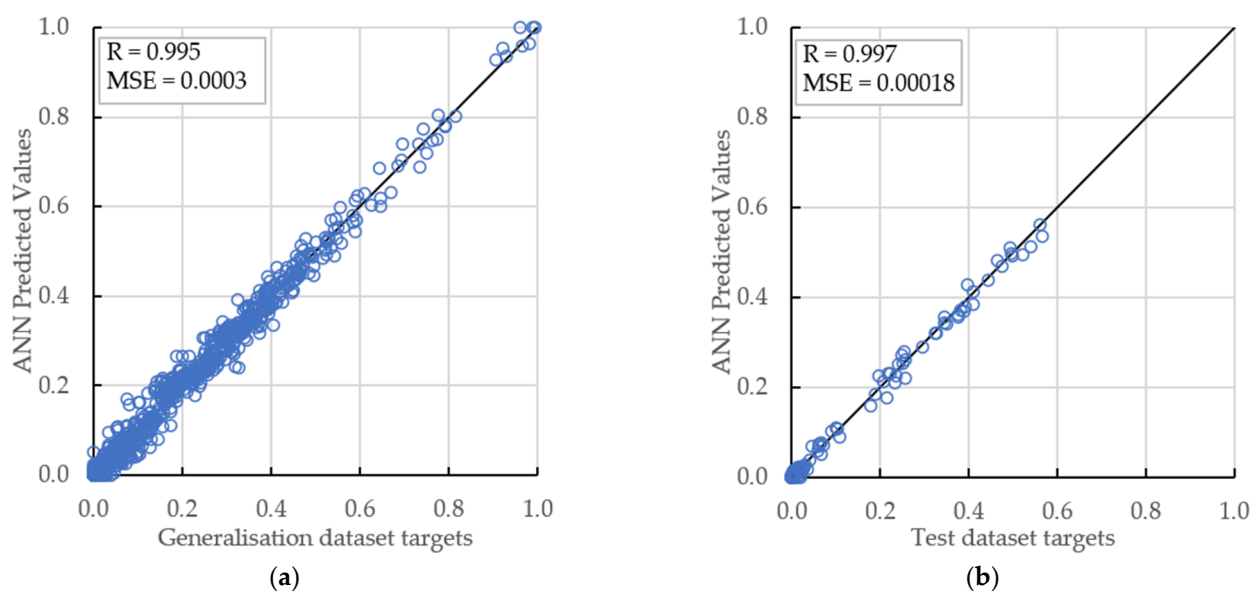
Figure 12. ANN-predicted values against the respective targets of the (**a**) generalisation dataset and (**b**) test dataset.

Table 3. Test dataset consisting of randomly selected sea-state events and absolute deviation of ANN predictions from targets.

Test Code No.	Sea State Events				Absolute Deviation (m)			
	H_s (m)	T_p (m)	MWD (°)	WL (m)	Port	Parking	Urban	Road
TS1	5.24	9.23	338.52	0.18	0.02	0.00	0.00	0.01
TS2	5.19	9.23	356.90	0.32	0.01	0.03	0.02	0.01
TS3	4.98	9.23	346.09	0.28	0.00	0.01	0.01	0.03
TS4	5.79	10.15	358.77	0.24	0.01	0.00	0.00	0.03
TR1	2.05	8.43	355.22	−0.27	0.00	0.01	0.00	0.01
TR2	2.14	7.15	359.63	0.40	0.01	0.01	0.00	0.00
TR3	2.28	8.46	337.71	0.16	0.00	0.00	0.00	0.02
TR4	2.32	6.05	354.88	−0.49	0.00	0.01	0.00	0.01
TR5	2.47	6.70	348.98	0.26	0.00	0.00	0.00	0.01
TR6	2.73	10.54	358.20	−0.46	0.01	0.01	0.00	0.01
TR7	2.88	8.97	310.59	−0.27	0.01	0.01	0.00	0.00
TR8	3.20	9.80	27.30	−0.06	0.00	0.04	0.02	0.00
TR9	3.22	7.04	6.80	−0.26	0.00	0.01	0.00	0.00
TR10	3.24	9.62	335.22	−0.19	0.01	0.01	0.02	0.00
TR11	3.76	9.34	303.46	−0.47	0.00	0.00	0.01	0.00
TR12	3.79	7.58	17.23	−0.21	0.00	0.04	0.02	0.02
TR13	3.80	8.29	354.93	−0.24	0.00	0.01	0.01	0.01
TR14	3.84	8.67	326.38	−0.01	0.02	0.01	0.02	0.02
TR15	5.83	10.02	346.64	−0.21	0.01	0.01	0.01	0.01
TR16	6.52	10.87	337.32	−0.30	0.02	0.00	0.00	0.03
TR17	6.62	10.11	326.43	−0.09	0.03	0.02	0.01	0.01
TR18	6.73	10.26	319.47	−0.43	0.03	0.03	0.02	0.00
min	2.05	6.05	6.80	−0.49	0.00	0.00	0.00	0.00
max	6.73	10.87	359.63	0.40	0.03	0.04	0.02	0.03

In Table 3, the absolute deviation between ANN-predicted values and test dataset targets is given for each event and each subarea of interest. The developed ANN delivered good results, given that the maximum deviation is 0.04 m. Figure 12b illustrates the ANN-predicted values, which favourably correlate with the respective targets of the test dataset with an *MSE* equal to 0.00018 and a correlation factor *R* equal to 0.997. In addition, to assess the resulting categorization of the coastal flood risk, Table 4 provides the respective risk for each event and each subarea of interest. It can be seen that the categorization of flood risk resulting from the ANN predicted values is the same as that derived from the test dataset targets, except for one event, namely, the TR17, and only for the urban subarea. In this case, the discrepancy concerning the predicted and test dataset risk category can be attributed to the specific threshold value adopted and does not stem from numerical errors in the simulations or insufficient training. More specifically, the flow depth value predicted from the ANN, equal to 0.355 m, is marginally above the adopted threshold of the high-risk category (i.e., 0.35 m), while the target, equal to 0.345 m, remained slightly lower, and is categorized as low risk.

Table 4. ANN predictions of coastal flood-risk level for randomly selected sea-state events.

Test Code No.	Coastal Flood Risk Categorization							
	Test Dataset Targets				ANN Predicted Values			
	Port	Parking	Urban	Road	Port	Parking	Urban	Road
TS1	3	3	2	2	3	3	2	2
TS2	2	3	3	2	2	3	3	2
TS3	2	3	2	2	2	3	2	2
TS4	3	3	3	3	3	3	3	3
TR1	1	1	1	1	1	1	1	1
TR2	1	1	1	1	1	1	1	1
TR3	1	1	1	1	1	1	1	1
TR4	1	1	1	1	1	1	1	1
TR5	1	1	1	1	1	1	1	1
TR6	1	1	1	1	1	1	1	1
TR7	1	1	1	1	1	1	1	1
TR8	1	2	1	1	1	2	1	1
TR9	1	1	1	1	1	1	1	1
TR10	1	2	2	1	1	2	2	1
TR11	1	2	1	1	1	2	1	1
TR12	1	2	1	1	1	2	1	1
TR13	1	2	1	1	1	2	1	1
TR14	1	3	2	1	1	3	2	1
TR15	3	3	2	2	3	3	2	2
TR16	3	3	2	2	3	3	2	2
TR17	3	3	2	2	3	3	3	2
TR18	3	3	2	1	3	3	2	1

As a final step of the present work, the ANN was applied to retrospectively deliver hourly sequential risk levels during flooding event S4 (occurred on 13 January 2015). According to the data obtained from the databases, during this occurrence, the offshore wave heights were ranged from 2 m to 5.8 m, the wave peak periods were between 6 s and 10 s, the MWD ranged from WNW (300°) to NNE (30°) and the water level elevation ranged from +0.10 m to +0.25 m from MWL. The resulting risk levels for the parking area are depicted in Figure 13. A medium-risk level appears on 12 January 2015 22:00 p.m. and high-risk levels initiate one hour later. The cessation of this event, according to the predictions of ANN, came almost 30 h later, i.e., on 14 January 2015 03:00 a.m., coinciding with the observations of the residents, who claimed that this event lasted more than a day.
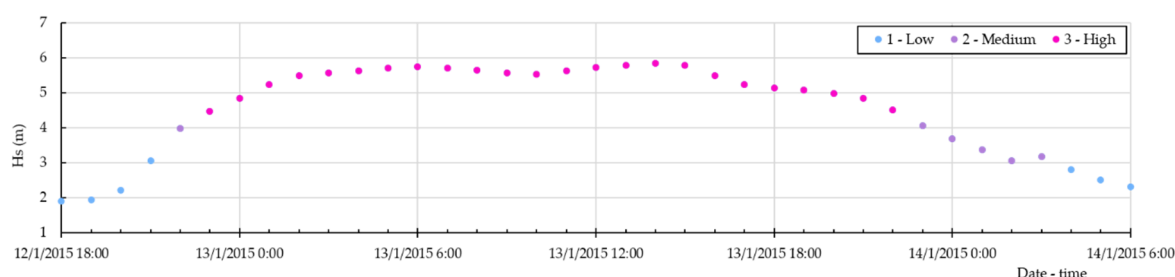
Figure 13. Coastal flood-risk levels in the parking area as predicted retrospectively by the developed ANN for the past flooding event S4 (occurred on 13 January 2015) in relation to offshore wave heights obtained from the open databases. Light blue dots represent a low-risk level, purple represent a medium-risk level and pink represent a high-risk level.

4. Discussion

Coastal floods constitute one of the most hazardous natural disasters, with often destructive consequences for the safety, properties and infrastructure of coastal communities. These hazards are intensified due to the climate change impacts inter-connected with the mean sea level rise as well as the more frequent occurrence of extreme storm surge and high-energy waves. Hence, the development of accurate early-warning systems of coastal flooding is of paramount importance to ensure the safety of coastal communities.

In the present research, a methodological approach to developing a coastal flood early-warning system, capable of producing accurate results in a time-effective manner, was proposed. One of the novel points of this early-warning system is that it only requires sea-state data (i.e., wave characteristics and sea level) offshore the study area as input and directly outputs the risk of imminent coastal flood in the coastal urban area. Sea-state data can be obtained from open databases offering forecasts spanning from a few hours up to the next seven days. Consequently, the EWS can offer predictions for the same timespan, without requiring intensive computational resources. This is achieved by the methodological approach proposed herein, which introduces an Artificial Neural Network trained with reliable data obtained by implementing a chain of high-credibility numerical models.

In principle, the proposed methodological approach remains valid for use in any coastal area up to the point where storm-induced erosion significantly alters the geomorphological characteristics of the coastal front, and nearby river outfalls, rainfall or urban water drainage begin to have a major impact on the coastal water level. Furthermore, it should be noted that the methodology is mainly suited for local scales and obviously relies upon the applied spatiotemporal analysis and the accuracy of the used open databaseforecasts.

The methodological approach introduced the Hindcast and the Forecast Frameworks. Implementation of the former ideally requires field measurements of flow depths and velocities but this is seldom the case. Therefore, field observations from video recordings and statements from local residents can contribute to validation of the applied numerical models according to past flooding events, which is of the utmost importance. It is also noted that in the context of the implementation of the Hindcast Framework in the present study, the data obtained from the considered open databases were close to reality, proving their reliability.

Regarding the Forecast Framework, some points are highlighted herein. Firstly, the selection of distinct sea state events is of crucial importance to properly train the ANN. In the present study, the incoming wave directions were broken down into 30-degree bins, wave heights were selected with an incremental step of 1.0 m, peak periods with a step of 1 s, and, finally, water levels were selected with a step of 0.5 m. Future research could contribute to the optimization of these steps, by selecting possibly greater values (e.g., a step of 1.5 m for wave heights) to reduce the events that need to be simulated (i.e., 303 herein) and simultaneously achieve an almost equal performance for the ANN. Secondly, regarding the training of the ANN, it is noted that fewer neurons and hidden layers resulted in low accuracy, while too many neurons and hidden layers increased the complexity without increasing the accuracy. It was observed that a double hidden layer produced an overall lower MSE and greater R in contrast with a single hidden layer; therefore, it is preferable. Thirdly, the testing process proved that the developed ANN delivered good results given that the absolute deviations of the predicted maximum flow depths from the respective targets generally remain close to zero, with the maximum deviation reaching a value of 0.04 m. Additionally, based on the results of the application of the developed ANN to deliver hourly sequential risk levels during a previous flooding event, we feel that the developed ANN could have warned the residents of Rethymno about the impending flood dangers if it had been available at the time. Finally, it is also important to state that the flood-risk categorization limits depend solely on the flow depths. Hence, future research should contribute to a more comprehensive categorization of coastal flood risks, distinguishing the risks that may arise on an island from the mainland and incorporating flow velocities,

the spatial extent of inundated areas, and coastal vulnerability, for instance by accounting for the vulnerability of different existing constructions.

Regarding the coastal area of Rethymno, waves with offshore heights equal to or greater than 3 m and peak wave periods equal or greater than 7 s can cause medium- to high-risk levels. The results of nearshore wave field simulations revealed that waves retain the largest proportion of their offshore energy when attacking the flood-prone coastal front, in contrast with the adjacent shores, where there is a wide breaker zone and waves reach the shoreline with significant energy loss. Waves coming from the N and NNW directions cause greater wave overtopping. As the mean annual frequency of occurrence of wave heights equal to or greater than 3 m is equal to 1.245% for the N direction and 0.114% for the NNW, it can be argued that the N direction causes the most coastal floods in the area of Rethymno. Furthermore, the elevated water levels substantially increase the risk, proving that storm surge plays a crucial role as a flood-driver in Rethymno, in contrast to the astronomical tide, which has a low range. Finally, according to the results, the largest overtopping volumes penetrate through the coastal front of the parking area, which is aligned with the visual observations of the residents.

Author Contributions: Conceptualization, M.C., A.M., C.M. and V.T.; methodology, M.C., A.M. and A.P.; software, M.C., A.M. and A.P.; validation, M.C., A.M., A.P. and V.T.; formal analysis, M.C., A.M. and A.P.; investigation, M.C., A.M. and A.P.; resources, M.C., A.M. and V.T.; data curation, M.C., A.M. and A.P.; writing—original draft preparation, M.C., A.M. and A.P.; writing—review and editing, M.C., A.M., A.P., C.M. and V.T.; visualization, M.C., A.M. and A.P.; supervision, V.T. and C.M.; project administration, M.C., A.M., A.P. and V.T.; funding acquisition, M.C., A.M., C.M. and V.T. All authors have read and agreed to the published version of the manuscript.

Conflicts of Interest: The authors declare no conflict of interest.

References

1. IPCC. Summary for Policy Makers. In *IPCC Special Report on the Ocean and Cryosphere in a Changing Climate*; Pörtner, H.O., Roberts, D.C., Masson-Delmotte, V., Zhai, P., Tignor, M., Poloczanska, E., Mintenbeck, K., Alegría, A., Nicolai, M., Okem, A., et al., Eds.; Cambridge University Press: Cambridge, UK; New York, NY, USA, 2019; In Press.
2. IPCC. Changes in climate extremes and their impacts on the natural physical environment. In *Managing the Risks of Extreme Events and Disasters to Advance Climate Change Adaptation*; Field, C.B., Barros, V., Stocker, T.F., Dahe, Q., Dokken, D.J., Ebi, K.L., Mastrandrea, M., Mach, K.J., Plattner, G.K., Allen, S.K., et al., Eds.; Cambridge University Press: Cambridge, UK; New York, NY, USA, 2012; pp. 109–230.
3. Petroliagkis, T.I.; Voukouvalas, E.; Disperati, J.; Bidlot, J. *Joint Probabilities of Storm Surge, Significant Wave Height and River Discharge Components of Coastal Flooding Events. Utilising Statistical Dependence Methodologies and Techniques, JCR Technical Reports*; Publications Office of the European Union: Luxembourg, 2016.
4. Tsoukala, V.K.; Chondros, M.; Kapelonis, Z.G.; Martzikos, N.; Lykou, A.; Belibassakis, K.; Makropoulos, C. An integrated wave modelling framework for extreme and rare events for climate change in coastal areas—The case of Rethymno, Crete. *Oceanologia* **2016**, *58*, 71–89. [CrossRef]
5. Gallien, T.; Sanders, B.; Flick, R. Urban coastal flood prediction: Integrating wave overtopping, flood defenses and drainage. *Coast. Eng.* **2014**, *91*, 18–28. [CrossRef]
6. Barnard, P.L.; Van Ormondt, M.; Erikson, L.H.; Eshleman, J.; Hapke, C.; Ruggiero, P.; Adams, P.; Foxgrover, A.C. Development of the Coastal Storm Modeling System (CoSMoS) for predicting the impact of storms on high-energy, active-margin coasts. *Nat. Hazards* **2014**, *74*, 1095–1125. [CrossRef]
7. Mendoza, E.T.; Jimenez, J.A. Regional vulnerability analysis of Catalan beaches to storms. In *Proceedings of the Institution of Civil Engineers—Maritime Engineering*; Thomas Telford Ltd.: London, UK, September 2009; Volume 162, pp. 127–135.

8.   Doong, D.-J.; Chuang, L.Z.H.; Wu, L.-C.; Fan, Y.-M.; Kao, C.C.; Wang, J.-H. Development of an operational coastal flooding early warning system. *Nat. Hazards Earth Syst. Sci.* **2012**, *12*, 379–390. [CrossRef]

9.   De Kleermaeker, S.; Verlaan, M.; Kroos, J.; Zijl, F. A new coastal flood forecasting system for the Netherlands. *Hydro12 Tak. Care Sea* **2012**, 13. [CrossRef]

10.   Bogaard, T.; De Kleermaeker, S.; Jaeger, W.S.; Van Dongeren, A. Development of Generic Tools for Coastal Early Warning and Decision Support. In *Proceedings of the E3S Web of Conferences*; EDP Sciences: Paris, France, 2016; Volume 7, p. 18017.

11.   Dreier, N.; Fröhle, P. Operational wave forecast in the German Bight as part of a sensor- and risk based early warning system. *J. Coast. Res.* **2018**, *85*, 1161–1165. [CrossRef]

12.   Winter, G.; Storlazzi, C.; Vitousek, S.; Van Dongeren, A.; McCall, R.; Hoeke, R.; Skirving, W.; Marra, J.; Reyns, J.; Aucan, J.; et al. Steps to Develop Early Warning Systems and Future Scenarios of Storm Wave-Driven Flooding Along Coral Reef-Lined Coasts. *Front. Mar. Sci.* **2020**, *7*, 199. [CrossRef]

13.   Merrifield, M.A.; Johnson, M.; Guza, R.T.; Fiedler, J.W.; Young, A.P.; Henderson, C.S.; Lange, A.M.Z.; O'Reilly, W.C.; Ludka, B.C.; Okihiro, M.; et al. An early warning system for wave-driven coastal flooding at Imperial Beach, CA. *Nat. Hazards* **2021**, *108*, 2591–2612. [CrossRef]

14.   Memos, C.; Makris, C.; Metallinos, A.; Karambas, T.; Zissis, D.; Chondros, M.; Spiliopoulos, G.; Emmanouilidou, M.; Papadimitriou, A.; Baltikas, V.; et al. Accu-Waves: A decision support tool for navigation safety in ports. In Proceedings of the 1st International Conference Design and Management of Port, Coastal and Offshore Works (DMPCO), Athens, Greece, 8–11 May 2019.

15.   Makris, C.; Androulidakis, Y.; Karambas, T.; Papadimitriou, A.; Metallinos, A.; Kontos, Y.; Baltikas, V.; Chondros, M.; Krestenitis, Y.; Tsoukala, V.; et al. Integrated modelling of sea-state forecasts for safe navigation and operational management in ports: Application in the Mediterranean Sea. *Appl. Math. Model.* **2020**, *89*, 1206–1234. [CrossRef]

16.   Spiliopoulos, G.; Bereta, K.; Zissis, D.; Memos, C.; Makris, C.; Metallinos, A.; Karambas, T.; Chondros, M.; Emmanouilidou, M.; Papadimitriou, A.; et al. A Big Data framework for Modelling and Simulating high-resolution hydrodynamic models in sea harbours. In Proceedings of the Global Oceans 2020: Singapore–USA Gulf Coast, Biloxi, MS, USA, 5–30 October 2020; IEEE: New York, NY, USA, 2020; pp. 1–5.

17.   Deo, M.C.; Jha, A.; Chaphekar, A.S.; Ravikant, K. Wave prediction using neural network. *Ocean Eng.* **2001**, *28*, 889–898. [CrossRef]

18.   Lee, T.-L. Neural network prediction of a storm surge. *Ocean Eng.* **2006**, *33*, 483–494. [CrossRef]

19.   Chondros, M.; Memos, C. Prediction of Wave Transmission Coefficient by Combining Experimental Measurements and Numerical Modelling. In Proceedings of the 4th International Conference on the Application of Physical Modelling to Port and Coastal Protection, Ghent, Belgium, 1 January 2012.

20.   Tsoukala, V.; Pyrpiri, T.; Chondros, M.; Katsardi, V. Prediction of wave transmission coefficient using neural networks and experimental measurements. In Proceedings of the 16th International Congress of the International Maritime Association of the Mediterranean IMAM 2015—Towards Green Marine Technology and Transport, Pula, Croatia, 21–24 September 2015.

21.   Doong, D.-J.; Peng, J.-P.; Chen, Y.-C. Development of a warning model for coastal freak wave occurrences using an artificial neural network. *Ocean Eng.* **2018**, *169*, 270–280. [CrossRef]

22.   Doong, D.-J.; Chen, S.-T.; Chen, Y.-C.; Tsai, C.-H. Operational Probabilistic Forecasting of Coastal Freak Waves by Using an Artificial Neural Network. *J. Mar. Sci. Eng.* **2020**, *8*, 165. [CrossRef]

23.   Mosavi, A.; Ozturk, P.; Chau, K.-W. Flood Prediction Using Machine Learning Models: Literature Review. *Water* **2018**, *10*, 1536. [CrossRef]

24.   Copernicus—Marine Environment Monitoring Service. Available online: https://marine.copernicus.eu/ (accessed on 15 January 2020).

25.   National Oceanographic and Atmospheric Adiminstration. Available online: https://www.ncdc.noaa.gov/data-access/ (accessed on 5 August 2021).

26.   AVISO. Available online: https://www.aviso.altimetry.fr/en/home.html (accessed on 5 August 2021).

27.   Jones, C.; Brøker, I.K.; Coulton, P.E.; Gangai, J.; Hatheway, D.; Lowe, J.; Noble, R.; Srinivas, R. *Wave Runup and Overtopping, FEMA Coastal Flood Hazard Analysis and Mapping Guidelines, Focused Study Report*; FEMA: Washington, DC, USA, 2005.

28.   Van der Meer, J.W.; Allsop, N.W.H.; Bruce, T.; De Rouck, J.; Kortenhaus, A.; Pullen, T.; Schüttrumpf, H.; Troch, P.; Zanuttigh, B. *EurOtop: Manual on Wave Overtopping of Sea Defences and Related Structures. An Overtopping Manual Largely Based on European Research, but for Worldwide Application*; Ghent University: Ghent, Belgium, 2016.

29.   Teng, J.; Jakeman, A.J.; Vaze, J.; Croke, B.F.W.; Dutta, D.; Kim, S. Flood inundation modelling: A review of methods, recent advances and uncertainty analysis. *Environ. Model. Softw.* **2017**, *90*, 201–216. [CrossRef]

30.   Rangel-Buitrago, N.; Anfuso, G. Review of the Existing Risk Assessment Methods. In *Risk Assessment of Storms in Coastal Zones: Case Studies from Cartagena (Colombia) and Cadiz (Spain)*; Springer Briefs in Earth Sciences; Springer: Berlin/Heidelberg, Germany, 2015; pp. 7–13.

31.   Ravdas, M.; Zacharioudaki, A.; Korres, G. Implementation and validation of a new operational wave forecasting system of the Mediterranean Monitoring and Forecasting Centre in the framework of the Copernicus Marine Environment Monitoring Service. *Nat. Hazards Earth Syst. Sci.* **2018**, *18*, 2675–2695. [CrossRef]

32. Escudier, R.; Clementi, E.; Drudi, M.; Pistoia, J.; Grandi, A.; Cipollone, A.; Lecci, R.; Omar, M.; Aydogdu, A.; Masina, S.; et al. A high resolution reanalysis for the Mediterranean Sea. In Proceedings of the 22nd EGU General Assembly, Online Event, 4–8 May 2020.
33. PEARL | Preparing for Extreme and Rare Events in CoastaL Regions. Available online: http://www.pearl-fp7.eu/ (accessed on 5 August 2021).
34. Chondros, M.K.; Metallinos, A.S.; Memos, C.D.; Karambas, T.V.; Papadimitriou, A.G. Concerted nonlinear mild-slope wave models for enhanced simulation of coastal processes. *Appl. Math. Model.* **2021**, *91*, 508–529. [CrossRef]
35. Kirby, J.T.; Dalrymple, R.A. A parabolic equation for the combined refraction–diffraction of Stokes waves by mildly varying topography. *J. Fluid Mech.* **1983**, *136*, 453–466. [CrossRef]
36. Kirby, J.T. A general wave equation for waves over rippled beds. *J. Fluid Mech.* **1986**, *162*, 171–186. [CrossRef]
37. Kirby, J.T. On the gradual reflection of weakly nonlinear Stokes waves in regions with varying topography. *J. Fluid Mech.* **1986**, *162*, 187–209. [CrossRef]
38. Miles, M.D.; Funke, E.R. A Comparison of Methods for Synthesis of Directional Seas. *J. Offshore Mech. Arct. Eng.* **1989**, *111*, 43–48. [CrossRef]
39. Van Gent, M.R.; Boogaard, H.F.V.D.; Pozueta, B.; Medina, J. Neural network modelling of wave overtopping at coastal structures. *Coast. Eng.* **2007**, *54*, 586–593. [CrossRef]
40. Verhaeghe, H.; De Rouck, J.; van der Meer, J. Combined classifier–quantifier model: A 2-phases neural model for prediction of wave overtopping at coastal structures. *Coast. Eng.* **2008**, *55*, 357–374. [CrossRef]
41. Mihu-Pintilie, A.; Cîmpianu, C.I.; Stoleriu, C.C.; Pérez, M.N.; Paveluc, L.E. Using High-Density LiDAR Data and 2D Streamflow Hydraulic Modeling to Improve Urban Flood Hazard Maps: A HEC-RAS Multi-Scenario Approach. *Water* **2019**, *11*, 1832. [CrossRef]
42. USACE. *HEC-RAS Hydraulic Reference Manual*; US Army Corps of Engineers: Davis, CA, USA, 2021.
43. Von Schuckmann, K.; Le Traon, P.Y.; Smith, N.; Pascual, A.; Djavidnia, S.; Gattuso, J.P.; Grégoire, M.; Aaboe, S.; Alari, V.; Alexander, B.E.; et al. Copernicus Marine Service Ocean State Report, Issue 5. *J. Oper. Oceanogr.* **2021**, *14*, 1–185. [CrossRef]